Helical buckling of thick-walled, pre-stressed, cylindrical tubes under a finite torsion*

Valentina Balbi and Pasquale Ciarletta†

Institut Jean le Rond d'Alembert, CNRS UMR 7190,
Université Pierre et Marie Curie - Paris 6,
4 place Jussieu, case 162, 75005 Paris, France

Abstract

We study the occurrence of torsional instabilities in soft, incompressible, thick-walled tubes with both circumferential and axial pre-stretches. Assuming a neo-Hookean strain energy function, we investigate the helical buckling under a finite torsion in three different classes of boundary conditions: a) no applied loads at the internal and external surfaces of the cylindrical tube, b) a pressure load P acting on the external surface or c) on the internal surface. We perform a linear stability analysis on the axisymmetric solutions using the method of small deformations superposed on finite strains. Applying a helical perturbation, we derive the Stroh formulation of the incremental boundary value problems and we solve it using a numerical procedure based on the surface impedance method. The threshold values of the torsion rate and the associated critical circumferential and longitudinal modes at the onset of the instability are examined in terms of the circumferential and axial pre-stretches, and of the initial geometry of the soft tube.

Keywords: Finite torsion, elastic stability, residual stresses, Stroh formulation, surface impedance method.

1 Introduction

A great impulse in the development of the modern theory of finite elasticity was given by the discovery of the existence of few universal solutions, i.e. which hold regardless of the specific form of the strain energy function. The finite torsion of a circular cylinder belongs to a special family of such universal solutions, as first reported by Rivlin for isotropic, incompressible, hyperelastic materials [1]. The application of a simple torsion to a cylindrical tube, in fact, defines an inhomogeneous deformation which is said to be controllable, meaning that it can be produced by surface tractions alone in the absence of external body forces [2]. The determination of all controllable deformations for isotropic, incompressible, hyperelastic bodies was first presented by Ericksen [3], and later extended to the wider class of simple materials [4–6]. Five families of inhomogeneous deformations have been identified, including the combined extension and torsion of a hollow cylinder [7]. For this case, further universal relations between the stress components have been reported by Ogden et al. [8] for a specific class of constitutive laws for rubber-like materials.

Although a bifurcation in the elastic stability occurs over a certain torsion rate for both solid and hollow cylinders, the observed instabilities in the two cases are very different. In fact, a twisted cylindrical rod immediately generates a kink, which suddenly forms a sharply bent ring [9], whilst a cylindrical tube

*This article is dedicated to Prof. R.W. Ogden on the occasion of his 70th birthday, as a token of gratitude for his seminal contributions in nonlinear elasticity.

†Corresponding author. E-mail: pasquale.ciarletta@upmc.fr

twisted beyond a critical torsion rate undergoes a helical buckling [10]. Very few studies have been performed to study such torsional instabilities in nonlinear elasticity. For solid cylinders, the basic homogeneous deformation allowed Green and Spencer [11] to provide analytical solutions for the torsion instability of a neo-Hookean material. Such a linear stability analysis was later extended to Mooney-Rivlin cylinders subjected to combined axial extension and finite torsion by the means of a numerical procedure [12]. For hollow cylinders, a linear elastic solution exists for cylindrical shells under a torsion load [13], whilst only Ertepinar and Wang [14] used nonlinear elasticity in order to find numerical results for thick-walled cylinders to be compared to a set of experimental tests. However, their model did not consider a basic elastic solution with radially inhomogeneous deformation, which in turn necessarily results from the absence of external traction loads at the side surfaces of the tube.

The aim of this work is to investigate the elastic stability of pre-stressed, hollow cylinders subjected to a finite torsion rate. We consider a hyperelastic, isotropic, neo-Hookean material and we take into account the presence of both axial and circumferential homogeneous pre-stretches as well as the incompressibility constraint, which are required to study the mechanical behavior of tubular living tissues [15,16]. The work is organized as follows. In Section 2, we describe the geometry and the kinematics of the elastic problem. In Section 3, we calculate the basic axisymmetric solutions considering three different sets of boundary conditions. When the faces of the tube are not subjected to an external pressure, we compute the fields for a radially inhomogeneous axisymmetric solution including extension and torsion. When one face is subjected to an external hydrostatic pressure, we specialize the analysis by considering a homogeneous pre-strain arising in response to pressure, followed by a finite torsion. The incremental elastic theory for the torsional instability is described in Section 4, and the results are presented in Section 5 and discussed in Section 6.

2 Geometry and kinematics of the elastic problem

Let $\mathcal{E} \subset \mathbb{R}^3$ be the three-dimensional Euclidean space, so that $\mathcal{B}_m, \mathcal{B}_a \subset \mathcal{E}$ are two regions occupied by a hollow circular cylinder in two different instants of time. In particular, we apply a finite torsion rate γ to the tube, which moves from the residually-stressed material configuration $\mathcal{B}_m$ to the spatial configuration $\mathcal{B}_a$. In order to take into account the presence of both circumferential and axial pre-stretch, we define the reference state $\mathcal{B}_0$ of the tube as a cylindrical sector with:

$$R_i \leq R \leq R_0, \quad 0 \leq \Theta \leq 2\pi - \beta, \quad 0 \leq Z \leq L \tag{1}$$

where R_i and R_0 are the inner and outer radii, respectively, L is the axial length and $\beta < 2\pi$ is the initial opening angle, as depicted in Figure 1. We remark that if β is positive one obtains an open cylindrical sector, whilst if it is negative there is an overlapping region in the reference state. Setting the orthonormal bases $(\mathbf{E}_R, \mathbf{E}_\Theta, \mathbf{E}_Z)$ in $\mathcal{B}_0$ and $(\mathbf{e}_r, \mathbf{e}_\theta, \mathbf{e}_z)$ in $\mathcal{B}_a$, we can define a mapping $\boldsymbol{\chi}$ as the following $\mathcal{C}^1$-diffeomorphism:

$$\boldsymbol{\chi} : \mathcal{B}_0 \to \mathcal{B}_a \qquad \mathbf{x} = \boldsymbol{\chi}(\mathbf{X}), \qquad \text{with inverse} \quad \mathbf{X} = \boldsymbol{\chi}^{-1}(\mathbf{x}) \tag{2}$$

from the reference position $\mathbf{X}$ in $\mathcal{B}_0$, into its spatial counterpart $\mathbf{x}$ in $\mathcal{B}_a$.

The mapping in equation (2) can be split into two components as $\boldsymbol{\chi} = \boldsymbol{\chi}_\gamma \circ \boldsymbol{\chi}_\lambda$, where $\boldsymbol{\chi}_\lambda$ is the component which restores the geometrical compatibility of the tube, therefore being associated with the definition of the circumferential and axial pre-stretches, and $\boldsymbol{\chi}_\gamma$ takes into account the application of a finite torsion rate, as shown in Figure 1.

Considering the cylindrical coordinate systems (r, θ, z) and (R, Θ, Z) in $\mathcal{B}_a$ and $\mathcal{B}_0$, respectively, let us define the mapping $\boldsymbol{\chi}$ using the following deformation fields:

$$\begin{cases} r(R, \Theta, Z) = r(R) \\ \theta(R, \Theta, Z) = \lambda_\theta \Theta + \lambda_z \gamma Z \\ z(R, \Theta, Z) = \lambda_z Z \end{cases} \tag{3}$$

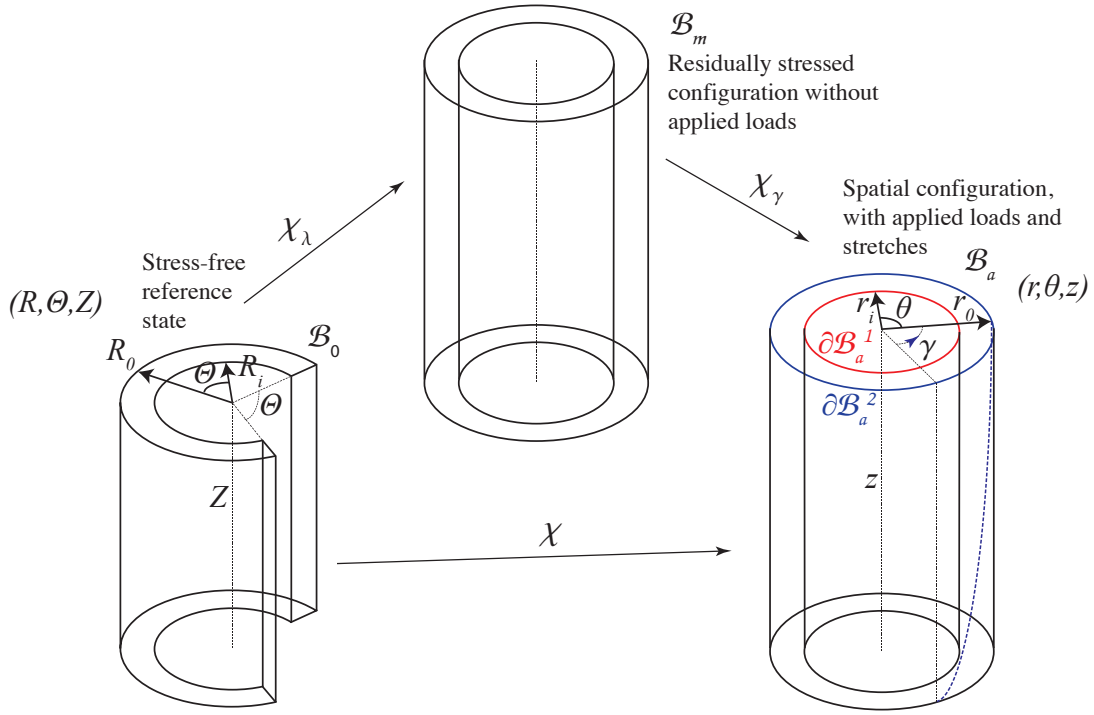

Figure 1: Schematic representation of the mapping $\boldsymbol{\chi}$: the component $\boldsymbol{\chi}_\lambda$ restores the geometrical compatibility mapping into the residually-stressed hollow cylinder in $\mathcal{B}_m$; while the component $\boldsymbol{\chi}_\gamma$ takes into account the finite torsion rate γ.

where $r(R)$ is a scalar function of R, $\lambda_\theta = 2\pi/(2\pi-\beta)$ is the circumferential pre-stretch, depending on the initial angle β, and γ is the finite torsion rate. Accordingly, the deformation gradient $\mathbf{F} = \mathrm{Grad}\,\boldsymbol{\chi}(\mathbf{X}) = \dfrac{\partial \boldsymbol{\chi}(\mathbf{X})}{\partial \mathbf{X}}$ associated to equation (3) is radially inhomogeneous and reads:

$$\mathbf{F} = \begin{pmatrix} \frac{\partial r(R)}{\partial R} & 0 & 0 \\ 0 & \dfrac{r}{R}\lambda_\theta & \lambda_z\gamma r \\ 0 & 0 & \lambda_z \end{pmatrix} \tag{4}$$

in the $\mathbf{E}_l \otimes \mathbf{e}_k$ basis, (l,k) spanning over $\{R,\Theta,Z\}$ and $\{r,\theta,z\}$, respectively. Furthermore, the local incompressibility constraint is given by:

$$\det \mathbf{F} = 1 \tag{5}$$

which, in its global form, allows to completely define the kinematics of the elastic problem, imposing:

$$r(R) = \sqrt{\frac{R^2}{\lambda_z\lambda_\theta} + a}, \qquad \text{with} \quad a = r_\mathrm{i}^2 - R_\mathrm{i}^2/(\lambda_\mathrm{z}\lambda_\theta). \tag{6}$$

Using equation (4), the left Cauchy-Green tensor $\mathbf{B} = \mathbf{F}\mathbf{F}^T$ reads:

$$\mathbf{B} = \begin{pmatrix} \left(\dfrac{R}{r\lambda_z\lambda_\theta}\right)^2 & 0 & 0 \\ 0 & \left(\dfrac{r}{R}\lambda_\theta\right)^2 + (\lambda_z\gamma r)^2 & \lambda_z^2\gamma r \\ 0 & \lambda_z^2\gamma r & \lambda_z^2 \end{pmatrix} \tag{7}$$

in the $\mathbf{e}_h \otimes \mathbf{e}_k$ basis, (h,k) spanning over $\{r,\theta,z\}$. As highlighted by Ogden [17], the Eulerian principal axes associated to the deformation in equation (3) have the following unit vectors:

$$\mathbf{e}_1 = \mathbf{e}_r, \quad \mathbf{e}_2 = \mathbf{e}_\theta \cos\phi - \mathbf{e}_z \sin\phi, \quad \mathbf{e}_3 = \mathbf{e}_\theta \sin\phi + \mathbf{e}_z \cos\phi, \tag{8}$$

where ϕ identifies the rotation angle of the principal vectors $\mathbf{e}_2$ and $\mathbf{e}_3$ with respect to $\mathbf{e}_\theta$ and $\mathbf{e}_z$. The corresponding principal stretches λ_1, λ_2 and λ_3 can be calculated by diagonalizing $\mathbf{B}$ as follows:

$$\mathbf{Q}^T \mathbf{B} \mathbf{Q} = \mathbf{V}^2 = \mathrm{diag}(\lambda_1^2, \lambda_2^2, \lambda_3^2) \tag{9}$$

where $\mathbf{Q}$ is the rotation matrix, associated to the change of basis in equation (8), diag indicates the diagonal matrix operator and $\mathbf{V}$ is the unique, positive-definite spatial stretch tensor arising from the polar decomposition of the deformation gradient. It follows that the principal stretch associated to the principal axes $\mathbf{e}_1$ is $\lambda_1 = \dfrac{R}{r\lambda_z\lambda_\theta}$, while the two other principal stretches are related by:

$$\begin{cases} \lambda_2^2 + \lambda_3^2 = \lambda_\theta^2 \dfrac{r^2}{R^2} + \lambda_z^2 \gamma^2 r^2 + \lambda_z^2 \\ \lambda_2 \lambda_3 = \dfrac{\lambda_z \lambda_\theta r}{R} \end{cases} \tag{10}$$

with:

$$\tan(2\phi) = \frac{2\lambda_z^2 \gamma r}{\lambda_2^2 + \lambda_3^2 - 2\lambda_z^2}, \tag{11}$$

which is valid within the range $0 \leqslant \phi < \pi/4$. In the next section, we introduce the constitutive assumption for the cylindrical tube and we derive the basic axisymmetric solutions for the torsion problem using three different sets of boundary conditions.

3 Constitutive assumption and basic axisymmetric solutions

Let us consider an isotropic, hyperelastic, incompressible material assuming a neo-Hookean strain energy function ψ:

$$\psi = \frac{\mu}{2}(\mathrm{tr}\,\mathbf{B} - 3) - p(\det \mathbf{F} - 1), \tag{12}$$

where μ is the shear modulus, p is the Lagrange multiplier arising when enforcing the incompressibility constraint, and tr is the trace operator. From equation (12), the constitutive relation for the nominal stress $\mathbf{S}$ and the Cauchy stress $\boldsymbol{\sigma} = \mathbf{SF}$ can be written as:

$$\mathbf{S} = \mu \mathbf{F}^T - p\mathbf{F}^{-1}; \qquad \boldsymbol{\sigma} = \mu \mathbf{B} - p\mathbf{I}. \tag{13}$$

Using equations (7, 13), the non-null components of the Cauchy stress tensor read:

$$\begin{cases} \sigma_{rr}(r) = \mu B_{rr} - p = \mu \dfrac{(r^2 - a)}{r^2 \lambda_\theta \lambda_z} - p \\ \sigma_{\theta\theta}(r) = \mu B_{\theta\theta} - p = \mu \left(\dfrac{r^2 \lambda_\theta}{\lambda_z (r^2 - a)} + \lambda_z \gamma r \right) - p \\ \sigma_{\theta z}(r) = \sigma_{z\theta}(r) = \mu B_{\theta z} = \mu \lambda_z^2 \gamma r \\ \sigma_{zz}(r) = \mu B_{zz} - p = \mu \lambda_z^2 - p. \end{cases} \tag{14}$$

It is useful to recall that, as first reported by Rivlin [1], the finite torsion of the pre-stretched cylinder can be obtained by applying surface tractions alone at the end surfaces, being:

$$N = 2\pi \int_{r_i}^{r_0} \sigma_{zz} r dr; \qquad M = 2\pi \int_{r_i}^{r_0} \sigma_{z\theta} r^2 dr \tag{15}$$

where N is a normal force and M is a torque, whose values depend on the applied boundary conditions. Moreover, the equilibrium equations in the spatial configuration are given by:

$$\operatorname{div} \boldsymbol{\sigma} = \mathbf{0} \qquad \text{in} \quad \mathcal{B}_a \tag{16}$$

where div is the spatial divergence operator. Substituting equation (14) into equation (16) , the equilibrium equations for an axisymmetric solution reduce to:

$$\frac{d\sigma_{rr}(r)}{dr} + \frac{1}{r}(\sigma_{rr}(r) - \sigma_{\theta\theta}(r)) = 0. \tag{17}$$

Considering the application of traction loads at the inner and outer surfaces, the most general expression of the boundary conditions reads:

$$\begin{cases} \boldsymbol{\sigma} \cdot \mathbf{n} = C_1 \mathbf{n} & \text{on} \quad \partial\mathcal{B}_a^1 = \{r : r = r_i\} \\ \boldsymbol{\sigma} \cdot \mathbf{n} = C_2 \mathbf{n} & \text{on} \quad \partial\mathcal{B}_a^2 = \{r : r = r_0\} \end{cases} \tag{18}$$

where $\mathbf{n}$ is the spatial outer normal unit vector on the surface and C_1, C_2 are two scalar values describing the presence of traction loads. As depicted in Figure 2, three sets of boundary conditions will be investigated in the following:

(a) no traction loads on the internal and external surfaces;

(b) a pressure of magnitude P acting on the external surface $\partial\mathcal{B}_a^1$;

(c) a pressure of magnitude P acting on the internal surface $\partial\mathcal{B}_a^2$.

whose corresponding values of the constants C_1, C_2 are collected in Table 1.

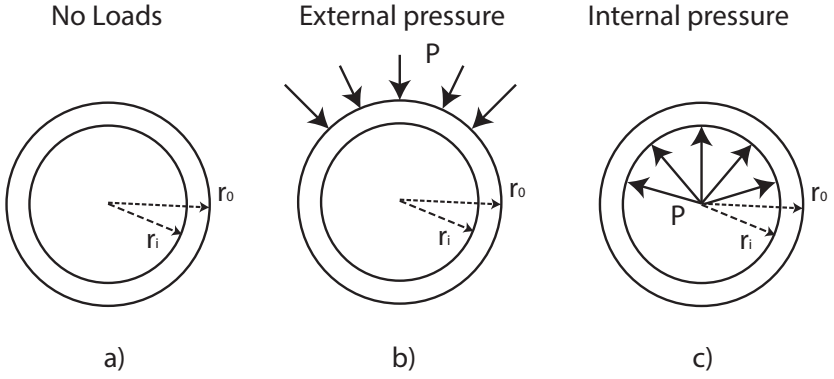

Figure 2: Three different boundary conditions are considered: the hollow cylinder (a) is stress-free at both surfaces, a pressure P is applied (b) at the external surface or (c) at the internal surface.

As discussed by Hoger [18], the distribution of residual stresses inside the material will depend not only on the shape of the body but also on the boundary conditions, which fix the Lagrange multiplier p. Therefore, we calculate the basic solution of the elastic problem expressed by in equations (16,18) for each of the three cases under consideration.

	on $r = r_i$	on $r = r_0$
(a) No loads	$C_1 = 0$	$C_2 = 0$
(b) External pressure	$C_1 = 0$	$C_2 = -P$
(c) Internal pressure	$C_1 = -P$	$C_2 = 0$

Table 1: Scalar values C_1, C_2 in equation (18), defining the boundary conditions of equation (16), for the three loading scenarios shown in Figure 2.

3.1 Case (a): stress-free internal and external surfaces

First, let us derive the basic axisymmetric solution of the equilibrium equation in equation (16), when no traction loads are applied on both the external and the internal surfaces of the cylindrical tube. In this case, the boundary conditions in equations (18) reduce to:

$$\begin{cases} \sigma_{rr}(r_i) = 0 \\ \sigma_{rr}(r_0) = 0 \end{cases} \tag{19}$$

Substituting equations (14) into equation (17), we get:

$$\int_{r_i}^{r_0} \frac{B_{rr}(r) - B_{\theta\theta}(r)}{r} dr = 0, \tag{20}$$

where the boundary conditions in equation (19) has been used. Recall that the relation between the deformed external and internal radii is given by the global incompressibility constraint in equation (6), reading here as:

$$r_0 = \sqrt{\frac{R_0^2 - R_i^2}{\lambda_z \lambda_\theta} + r_i^2}. \tag{21}$$

By substituting r_0 from equation (21) into equation (20) we get:

$$\frac{1}{H^2 \lambda_\theta^2} \left(\frac{1}{r_i^2 \lambda_z} - \gamma^2 (H^2 - 1) \lambda_\theta \lambda_z^2 - \frac{H^4 \lambda_\theta}{H^2 + H^2 r_i^2 \lambda_\theta \lambda_z - 1} \right) - 2\lambda_\theta \log[H] + \frac{1}{\lambda_\theta} \log \left[1 + \frac{H^2 - 1}{H^2 r_i^2 \lambda_\theta \lambda_z} \right] = 0, \tag{22}$$

where $H = R_0/R_i$ is the initial aspect ratio. equation (22) defines an implicit relation to derive the deformed internal radius r_i, and, consequently, r_0 from equation (21), given the initial geometry of the hollow tube, the axial and circumferential pre-stretches and the finite torsion rate. The variation of r_i and r_0 with the initial aspect ratio is depicted in Figure 3 (left), showing the curves obtained by numerically solving, for a given choice of β, λ_z and γ, equations (21, 22) using the Newton method. Finally, the Lagrange multiplier p can be easily calculated from equation (17), using equation (21), and reads:

$$p = \mu B_{rr}(r) + \mu \int_r^{r_0} \frac{B_{rr}(s) - B_{\theta\theta}(s)}{s} ds, \tag{23}$$

which allows to calculate the distribution of the Cauchy stress components inside the tube. In Figure 3 (right) the distribution of the radial and circumferential components of the Cauchy stress are depicted as functions of the radius. The residual circumferential stress is compressive at the internal radius and tensile at the external radius, while the radial component is always compressive across the layer and it vanishes at the internal and external surfaces for the boundary conditions.

3.2 Case (b): Pressure load P at the external surface

Let us now solve the equilibrium equations in equation (16), when a pressure of load P acts on the external surface of the cylindrical tube. In detail, we focus on the particular case in which the residual

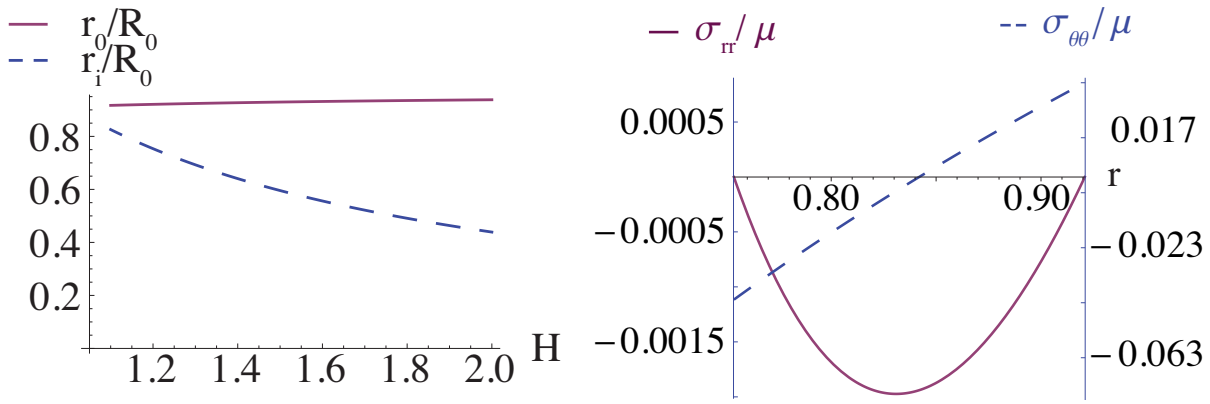

Figure 3: External and internal radii, r_0 (thick) and r_i (dashed), respectively, plotted against the initial aspect ratio $H = R_0/R_i$ (left); and Cauchy stress components σ_{rr} (thick) and $\sigma_{\theta\theta}$ (dashed) within a tube with initial aspect ratio $H = 1.2$ (right). The curves are obtained setting $\beta = \pi/6$, $\lambda_z = 1$, and $\gamma = 0.15$, for traction-free internal and external surfaces.

strains arise in response to the applied pressure in order to provide an optimal material behavior. Such a stress-adaptation is typical of biological tissues, as investigated by Destrade et al. [19] based on a previous study on arteries [20], where the physiological amount of circumferential pre-stretch is naturally calibrated in order to induce a homogeneous deformation inside the tissue under the action of the blood pressure. Using the same idea, in the absence of a torsion rate we assume that the tube undergoes the following homogeneous deformation when a pressure P is applied on the external surface of the cylinder:

$$r^h(R,\Theta,Z) = \frac{R}{\sqrt{\lambda_z\lambda_\theta}}; \quad \theta^h(R,\Theta,Z) = \lambda_\theta\Theta; \quad z^h(R,\Theta,Z) = \lambda_z Z. \tag{24}$$

giving rise to the homogeneous deformation gradient:

$$\mathbf{F}^h = \mathrm{diag}\left(\frac{1}{\sqrt{\lambda_z\lambda_\theta}}, \sqrt{\frac{\lambda_\theta}{\lambda_z}}, \lambda_z\right) \tag{25}$$

Accordingly, the boundary conditions allow to derive an analytical relationship between the external pressure P and the pre-strains inside the tube:

$$P = \mu\int_{r_i}^{r_0} \frac{{F^h_{rr}}^2(r) - {F^h_{\theta\theta}}^2(r)}{r}dr = -\frac{(-1+\lambda_\theta^2)\mu\ln[H]}{\lambda_\theta\lambda_z}, \tag{26}$$

If we consider an applied pressure P given by equation (26) at the external surface, the boundary conditions in equation (18) read as:

$$\begin{cases} \sigma_{rr}(r_i) = 0 \\ \sigma_{rr}(r_0) = -P = \dfrac{(-1+\lambda_\theta^2)\mu\ln[H]}{\lambda_\theta\lambda_z}. \end{cases} \tag{27}$$

Accordingly, the Lagrange multiplier p can be calculated from equation (17), using the inhomogeneous deformation fields in equation (3), as follows:

$$p = \mu B_{rr}(r) - \mu\int_{r}^{r_0} \frac{B_{rr}(r) - B_{\theta\theta}(r)}{r}dr - \frac{(-1+\lambda_\theta^2)\mu\ln[H]}{\lambda_\theta\lambda_z}, \tag{28}$$

where r_0 is given by equation (21). As in the previous case, the internal radius r_i is implicitly calculated from the boundary conditions in equation (27), using equations (14, 17). The variations of the radial and circumferential components of the Cauchy stress with r are depicted in Figure 4 (left).

3.3 Case (c): Pressure load P at the internal surface

Finally, let us consider the case of a pressure load P applied on the internal surface of the cylindrical tube only. Making the same assumptions used for the case (b), the internal pressure is related to the pre-strains of the tube by the following relation:

$$P = -\int_{r_i}^{r_0} \frac{\sigma_{rr}(r) - \sigma_{\theta\theta}(r)}{r} dr = \frac{(-1+\lambda_\theta^2)\mu \ln[H]}{\lambda_\theta \lambda_z}. \tag{29}$$

In this case, the boundary conditions in equation (18) read:

$$\begin{cases} \sigma_{rr}(r_i) = -P = \dfrac{(1-\lambda_\theta^2)\mu \ln[H]}{\lambda_\theta \lambda_z} \\ \sigma_{rr}(r_0) = 0. \end{cases} \tag{30}$$

Finally, the Lagrange multiplier p is obtained by solving the equilibrium problem in equation (17) with boundary conditions in equation (30), being:

$$p = \mu B_{rr}(r) + \mu \int_{r_i}^{r} \frac{B_{rr}(r) - B_{\theta\theta}(r)}{r} dr + \frac{(-1+\lambda_\theta^2)\mu \ln[H]}{\lambda_\theta \lambda_z}, \tag{31}$$

where r_i is calculated substituting equations (14,17) into the boundary conditions in equation (30). The radial and circumferential components of the Cauchy stress for the case (c) are depicted in Figure 4 (right).

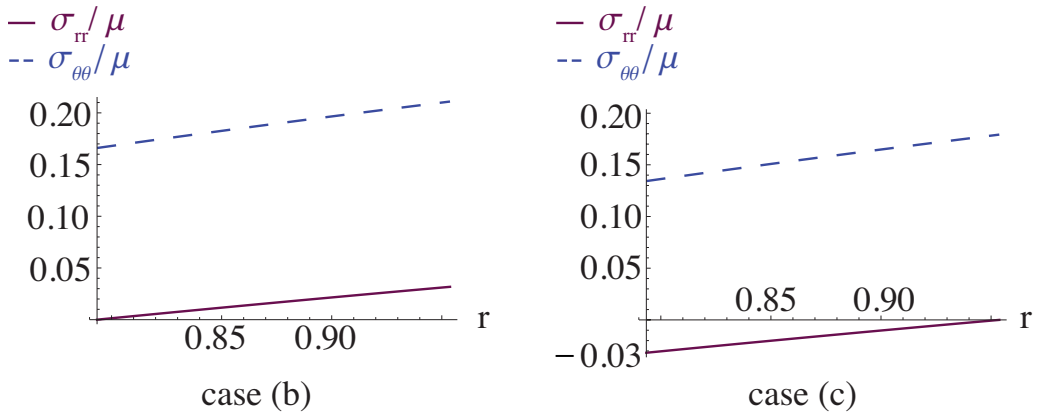

Figure 4: Cauchy stress components σ_{rr} (thick) and $\sigma_{\theta\theta}$ (dashed) within a tube with initial aspect ratio $H = 1.2$. The curves are obtained setting $\beta = \pi/6$, $\lambda_z = 1$, and $\gamma = 0.15$, when a pressure is applied at the external (left) and internal (right) surface.

For the given pre-stretches, the resulting circumferential stresses have the same sign for both cases, but the maximum stress is higher for the case (b), suggesting an earlier onset of the instability. Moreover, the radial stress is tensile across the layer in the case (b), whilst it is compressive in the case (c).

In the following section, we perform a linear stability analysis of the axisymmetric elastic solutions to study the onset of torsional instabilities for the hollow cylinder.

4 Linear stability analysis

Here the stability of the hollow cylinder subjected to finite torsion is investigated using the method of incremental deformations superposed on finite strains [17]. First, we define a perturbation of the basic axisymmetric solutions and, second, we solve the associated incremental problem for calculating the critical values for the torsion rate at the onset of the torsional instability.

4.1 Definition of the incremental deformation

Let us define an infinitesimal perturbation $\delta\mathbf{x}$ of the basic solution $\mathbf{x}$ as follows:

$$\bar{\mathbf{x}} = \mathbf{x} + \delta\mathbf{x} = \boldsymbol{\chi}(\mathbf{X}) + \boldsymbol{\chi}^{(1)}(\mathbf{x}), \tag{32}$$

where $\bar{\mathbf{x}}$ is the perturbed position vector, and $\boldsymbol{\chi}^{(1)} : \mathcal{B}_a \to \mathcal{B}'_a$ is the incremental mapping that takes the spatial position vector $\mathbf{x}$ into the perturbed configuration $\mathcal{B}'_a \subset \mathcal{E}$. If the displacement vector $\delta\mathbf{x}$ satisfies the condition $|\delta\mathbf{x}|^2 \ll |\delta\mathbf{x}|, \forall\mathbf{x} \in \mathcal{B}_a$, then we can refer to $\boldsymbol{\chi}^{(1)}$ as an incremental deformation. The incremental displacement vector $\delta\mathbf{x}$, can be expressed as:

$$\delta\mathbf{x} = \boldsymbol{\chi}^{(1)}(r,\theta,z) = u(r,\theta,z)\mathbf{e}_r + v(r,\theta,z)\mathbf{e}_\theta + w(r,\theta,z)\mathbf{e}_z \tag{33}$$

where u, v, w are three incremental displacement fields. Accordingly, the spatial displacement gradient associated to the incremental deformation, $\boldsymbol{\Gamma} = \operatorname{grad}\boldsymbol{\chi}^{(1)}(\mathbf{x}) = \dfrac{\partial\boldsymbol{\chi}^{(1)}(\mathbf{x})}{\partial\mathbf{x}}$, reads:

$$\boldsymbol{\Gamma} = \begin{pmatrix} u_{,r} & (u_{,\theta} - v)/r & u_{,z} \\ v_{,r} & (v_{,\theta} + u)/r & v_{,z} \\ w_{,r} & (v_{,\theta})/r & w_{,z} \end{pmatrix} \tag{34}$$

in the $\mathbf{e}_l \otimes \mathbf{e}_k$ basis, (l,k) spanning over $\{r,\theta,z\}$. where the comma denotes the partial differentiation with respect to the argument.

In the following, we will use barred variables in order to identify the perturbed quantities. From equation (32), the perturbed deformation gradient $\bar{\mathbf{F}}$ reads:

$$\bar{\mathbf{F}} = \mathbf{F} + \delta\mathbf{F} = \mathbf{F} + \boldsymbol{\Gamma}\mathbf{F}, \tag{35}$$

where $\delta\mathbf{F}$ is the increment of the basic deformation gradient $\mathbf{F}$. The perturbed nominal stress is given by:

$$\bar{\mathbf{S}} = \mathbf{S} + \dot{\mathbf{S}} \tag{36}$$

where $\mathbf{S}$ is the basic nominal stress in equation (13) and $\dot{\mathbf{S}}$ is its increment, which can calculated by simple differentiation rules.

In particular, its push-forward of $\dot{\mathbf{S}}_0$ in the perturbed configuration reads:

$$\dot{\mathbf{S}}_0 = \mathbf{F}\dot{\mathbf{S}} = \boldsymbol{\mathcal{A}}_0^1\boldsymbol{\Gamma} + p\boldsymbol{\Gamma} - q\mathbf{I} \tag{37}$$

where q is the increment of the Lagrange multiplier p, and $\boldsymbol{\mathcal{A}}_0^1$ is the so called tensor of instantaneous moduli, which is given by:

$$\mathcal{A}^1_{0hklj} = F_{h\iota}F_{l\beta}\frac{\partial^2\psi}{\partial F_{k\iota}\partial F_{j\beta}} = \mu\delta_{kj}B_{hl}, \tag{38}$$

where δ_{kj} is the Kronecker delta and equation (12) has been used. The incremental equilibrium equations in the spatial form can be written as:

$$\begin{cases} \operatorname{div}\dot{\mathbf{S}}_0 = \mathbf{0} & \text{in} \quad \mathcal{B}'^1_a \\ \dot{\mathbf{S}}_0^T \cdot \mathbf{n} = \delta C_1\mathbf{n} - C_1\boldsymbol{\Gamma}^T\mathbf{n} & \text{on} \quad \partial\mathcal{B}'^1_a \\ \dot{\mathbf{S}}_0^T \cdot \mathbf{n} = \delta C_2\mathbf{n} - C_2\boldsymbol{\Gamma}^T\mathbf{n} & \text{on} \quad \partial\mathcal{B}'^2_a \end{cases} \tag{39}$$

where $\dot{\mathbf{S}}_0$ is given by equation (37) and $\delta C_1, \delta C_2$ are the increments of the boundary values C_1, C_2, respectively. Furthermore, the incremental incompressibility constraint reads:

$$\operatorname{tr} \mathbf{\Gamma} = 0. \tag{40}$$

In summary, the bulk equations of the incremental boundary value problem are given by a system of four partial differential equations (PDEs), i.e. the three incremental equilibrium equations in equation (39):

$$\begin{aligned}
&\frac{\partial(r\dot{S}_{0rr})}{\partial r} + \frac{\partial \dot{S}_{0\theta r}}{\partial \theta} + r\frac{\partial \dot{S}_{0zr}}{\partial z} - \dot{S}_{0\theta\theta} = 0 \\
&\frac{\partial(r\dot{S}_{0r\theta})}{\partial r} + \frac{\partial \dot{S}_{0\theta\theta}}{\partial \theta} + r\frac{\partial \dot{S}_{0z\theta}}{\partial z} + \dot{S}_{0\theta r} = 0 \\
&\frac{\partial(r\dot{S}_{0rz})}{\partial r} + \frac{\partial \dot{S}_{0\theta z}}{\partial \theta} + r\frac{\partial \dot{S}_{0zz}}{\partial z} = 0
\end{aligned} \tag{41}$$

and the incremental incompressibility condition in equation (40):

$$u_{,r} + \frac{u + v_{,\theta}}{r} + w_{,z} = 0. \tag{42}$$

In the next section, we rewrite the incremental elastic problem in equations (39,40) into the more convenient Stroh formulation.

4.2 Stroh formulation

The Stroh formulation allows to transform the system of four PDEs in equations (41,42) with boundary conditions in equation (39) into a system of six ordinary differential equations (ODEs) with given initial conditions [21].

Assuming variable separation, we consider the following expression of the incremental displacements:

$$\begin{aligned}
\{u, q\} &= \{U(r), Q(r)\}\cos(k_z z - m\theta) \\
\{v, w\} &= \{V(r), W(r)\}\sin(k_z z - m\theta)
\end{aligned} \tag{43}$$

where m is the circumferential mode and $k_z = 2n\pi/L$ is the wavenumber of the tube in the longitudinal direction, with m and n being integers, and U, V, W, Q are four scalar functions of r. Such a helical perturbation deforms the hollow cylinder as illustrated in Figure 5.

From equation (37) and equation (43), the incremental stress components must have the following form:

$$\begin{aligned}
\dot{S}_{0rr} &= S_{0rr}(r)\cos(k_z z - m\theta) \\
\{\dot{S}_{0r\theta}, \dot{S}_{0rz}\} &= \{S_{0r\theta}(r), S_{0rz}(r)\}\sin(k_z z - m\theta)
\end{aligned} \tag{44}$$

where $S_{0rr}, S_{0r\theta}, S_{0rz}$ are three scalar functions of r. Substituting equations (43-44) into the incremental constitutive equations in equation (37), we obtain:

$$Q = (\mathcal{A}^1_{0rrrr} + p)U' - S_{0rr} \tag{45}$$

$$V' = \frac{S_{0r\theta}}{\mathcal{A}^1_{0r\theta r\theta}} + \frac{1}{r}\frac{(V - mU)}{\mathcal{A}^1_{r\theta r\theta}}p \tag{46}$$

$$W' = \frac{S_{0rz}}{\mathcal{A}^1_{0rzrz}} + \frac{k_z U}{\mathcal{A}^1_{0rzrz}}p, \tag{47}$$

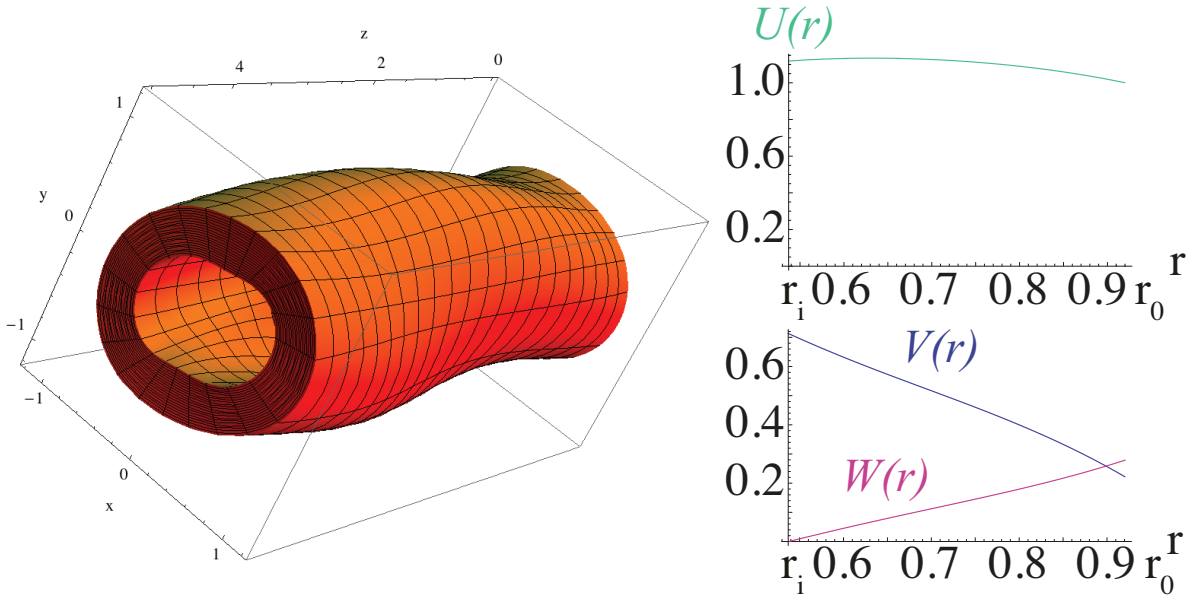

Figure 5: Helical buckling of a cylindrical tube obtained from the output of the numerical simulations in the case (a) for $H = 1.6$, $R_0 = 1$, $L = 5$, $U(r_0) = 0.15$ $\lambda_z = 1$ and $\beta = \pi/6$, occurring at the critical wavenumbers $m = 2$, $k_z = 1.37$ (left). Plots of the resulting incremental displacement fields $U(r)$, $V(r)$ and $W(r)$ inside the tube, setting $U(r_0) = 1$ (right). The amplitude of the linear perturbation is fixed arbitrarily for illustrative purposes.

where the prime denotes differentiation. Moreover, the incremental incompressibility condition in equation (42), reads:

$$U' = \frac{mV - U}{r} - k_z W. \tag{48}$$

Substituting equations (37) and (43) into equations (41), and using equation (44) to replace the components $\dot{S}_{0rr}, \dot{S}_{0r\theta}, \dot{S}_{0rz}$ of the incremental stresses, we get:

$$\begin{aligned}
&\frac{1}{r^2}\Big\{-rS_{0rr} - \Big[\mathcal{A}^1_{0\theta\theta\theta\theta} + \mathcal{A}^1_{0\theta r\theta r}m^2 + p + k_z r\Big(-m\mathcal{A}^1_{0\theta rzr} - m\mathcal{A}^1_{0zr\theta r} + \mathcal{A}^1_{0zrzr}k_z r\Big)\Big]U \\
&+\Big[m\Big(\mathcal{A}^1_{0\theta r\theta r} + \mathcal{A}^1_{0\theta\theta\theta\theta} + p\Big) - \Big(\mathcal{A}^1_{0\theta\theta z\theta} + \mathcal{A}^1_{0zr\theta r}\Big)k_z r\Big]V \\
&+r\Big[\Big(rS_{0rr}\Big)' + \Big(\mathcal{A}^1_{0rrrr} + p\Big)U' - mpV'\Big] + k_z p r^2 W'\Big\} = 0,
\end{aligned} \tag{49}$$

$$\begin{aligned}
&\frac{1}{r^2}\Big\{ - m\Big(rS_{0rr}\Big) - \Big[m\Big(\mathcal{A}^1_{0\theta r\theta r} + \mathcal{A}^1_{0\theta\theta\theta\theta} + p\Big) - \Big(\mathcal{A}^1_{0\theta rzr} + \mathcal{A}^1_{0z\theta\theta\theta}\Big)k_z r\Big]U \\
&+\Big[\mathcal{A}^1_{0\theta r\theta r} + m^2\Big(\mathcal{A}^1_{0\theta\theta\theta\theta} + p\Big) - \Big(\mathcal{A}^1_{0\theta\theta z\theta} + \mathcal{A}^1_{0z\theta\theta\theta}\Big)k_z mr + \mathcal{A}^1_{0z\theta z\theta}k_z^2 r^2\Big]V \\
&-k_z mprW - r\Big(rS_{0rt}\Big)' + \mathcal{A}^1_{0rrrr}mrU' + mprU' - prV'\Big\} = 0,
\end{aligned} \tag{50}$$

$$\frac{1}{r^2}\Bigg\{k_z r\Big(rS_{0rr}\Big) - k_z mprV + \Big[\mathcal{A}^1_{0\theta z\theta z}m^2 + k_z^2\Big(\mathcal{A}^1_{0zzzz}+p\Big)r^2 - \Big(\mathcal{A}^1_{0\theta zzz}+\mathcal{A}^1_{0zz\theta z}\Big)mk_z r\Big]W$$
$$-r\Big(rS_{0rz}\Big)' - k_z\Big(\mathcal{A}^1_{0rrrr}+p\Big)r^2U'\Bigg\} = 0. \tag{51}$$

Now, let us define the displacement-traction vector $\boldsymbol{\eta}$, as follows:

$$\boldsymbol{\eta}(r) = \left[\begin{array}{c} \mathbf{U}(r) \\ r\mathbf{S}(r) \end{array}\right]; \quad \text{with} \quad \left\{\begin{array}{l} \mathbf{U}(r) = [U(r), V(r), W(r)]^T \\ \mathbf{S}(r) = [S_{0rr}(r), S_{0r\theta}(r), S_{0rz}(r)]^T \end{array}\right. \tag{52}$$

Accordingly, equations (46-51) can be compactly rewritten as:

$$\frac{d\boldsymbol{\eta}(r)}{dr} = \frac{1}{r}\mathbf{G}(r)\boldsymbol{\eta}(r), \tag{53}$$

where $\mathbf{G}$ is the so-called Stroh matrix, having the following block form:

$$\mathbf{G} = \left(\begin{array}{cc} \mathbf{G}_1 & \mathbf{G}_2 \\ \mathbf{G}_3 & \mathbf{G}_4 \end{array}\right). \tag{54}$$

In particular, the four blocks of $\mathbf{G}$ read:

$$\mathbf{G}_1 = \left(\begin{array}{ccc} -1 & m & -k_z r \\ -m\sigma_1 & \sigma_1 & 0 \\ k_z r\sigma_2 & 0 & 0 \end{array}\right), \quad \mathbf{G}_2 = \left(\begin{array}{ccc} 0 & 0 & 0 \\ 0 & 1/\alpha_1 & 0 \\ 0 & 0 & 1/\alpha_2 \end{array}\right), \tag{55}$$

$$\mathbf{G}_3 = \left(\begin{array}{ccc} \kappa_{11} & \kappa_{12} & \kappa_{13} \\ \kappa_{12} & \kappa_{22} & -\kappa_{23} \\ \kappa_{13} & -\kappa_{23} & \kappa_{33} \end{array}\right), \quad \mathbf{G}_4 = -\mathbf{G}_1^T, \tag{56}$$

where:

$$\begin{aligned}
\kappa_{11} &= m^2(\nu_1 - \alpha_1\sigma_1^2) + k_z^2 r^2(\nu_2 - \alpha_2\sigma_2^2) + (\mathcal{A}^1_{0rrrr} + \mathcal{A}^1_{0\theta\theta\theta\theta}) + 2\alpha_1\sigma_1 - k_z rm(\mathcal{A}^1_{0\theta rzr} + \mathcal{A}^1_{0zr\theta r}), \\
\kappa_{12} &= m\Big\{-\mathcal{A}^1_{0rrrr} - \mathcal{A}^1_{0\theta\theta\theta} - \nu_1 + \alpha_1\big[(\sigma_1-1)^2 - 1\big]\Big\} + k_z r(\mathcal{A}^1_{0\theta\theta z\theta} + \mathcal{A}^1_{0zr\theta r}), \\
\kappa_{13} &= k_z r(\mathcal{A}^1_{0rrrr} + \alpha_1\sigma_1), \\
\kappa_{22} &= m^2\big[(\mathcal{A}^1_{0rrrr} + \mathcal{A}^1_{0\theta\theta\theta}) + 2\alpha_1\sigma_1\big] - k_z rm(\mathcal{A}^1_{0\theta\theta z\theta} + \mathcal{A}^1_{0z\theta\theta\theta}) + k_z^2 r^2\nu_3 + \nu_1 - \sigma_1^2\alpha_1, \\
\kappa_{23} &= mk_z r(\mathcal{A}^1_{0rrrr} + 2\alpha_1\sigma_1), \\
\kappa_{33} &= m^2\alpha_3 + k_z^2 r^2(\mathcal{A}^1_{0rrrr} + \mathcal{A}^1_{0zzzz} + 2\alpha_3\sigma_3) - k_z rm(\mathcal{A}^1_{0\theta zzz} + \mathcal{A}^1_{0zz\theta z}),
\end{aligned} \tag{57}$$

and:

$$\begin{array}{lll}
\nu_1 = A^1_{0\theta r\theta r}, & \alpha_1 = \mathcal{A}^1_{0r\theta r\theta}, & \sigma_1 = p/\alpha_1, \\
\nu_2 = A^1_{0zrzr}, & \alpha_2 = \mathcal{A}^1_{0rzrz}, & \sigma_2 = p/\alpha_2, \\
\nu_3 = A^1_{0z\theta z\theta}, & \alpha_3 = \mathcal{A}^1_{0\theta z\theta z}, & \sigma_3 = p/\alpha_3
\end{array} \tag{58}$$

In the next paragraph, we introduce the surface impedance method to build a numerical procedure for solving equation (53) with the three sets of boundary conditions in Table 1.

4.3 The surface impedance method

The surface impedance method is usually employed to study propagation of surface waves in inhomogeneous media [22, 23] and was recently adapted to cylindrically geometries [24]. Let $\boldsymbol{\eta}_l(r)$, with

$l = \{1, \ldots, 6\}$ be a set of independent solutions of the system in equation (53), and let $\boldsymbol{\mathcal{N}}$ be the integral matrix, defined as:

$$\boldsymbol{\mathcal{N}}(r) = [\boldsymbol{\eta}_1, \ldots, \boldsymbol{\eta}_6]\,. \tag{59}$$

Let us define the 6x6 matricant solution $\mathbf{M}(r, r_k)$, $(k = i, o)$ as the block matrix:

$$\mathbf{M}(r, r_k) = \begin{pmatrix} \mathbf{M}_1(r, r_k) & \mathbf{M}_2(r, r_k) \\ \mathbf{M}_3(r, r_k) & \mathbf{M}_4(r, r_k) \end{pmatrix} = \boldsymbol{\mathcal{N}}(r)\boldsymbol{\mathcal{N}}^{-1}(r_k), \tag{60}$$

which, from equation (53), is the solution of the initial value problem:

$$\frac{d\mathbf{M}}{dr}(r, r_k) = \mathbf{G}(r)\mathbf{M}(r, r_k), \quad \text{with} \quad \mathbf{M}(r_k, r_k) = \mathbf{I}_{(6)}, \tag{61}$$

where $\mathbf{I}_{(6)}$ is the 6x6 identity matrix. The conditional impedance matrix $\mathbf{z} = \mathbf{z}(r, r_k)$ can be defined as the 3x3 matrix, such that

$$r\mathbf{S} = \mathbf{z}\mathbf{U}, \tag{62}$$

where the term "conditional" refers to the dependence on the boundary condition at $r = r_k$. In fact, if a zero traction condition is assumed at $r = r_k$, then $\mathbf{z}$ has the following form:

$$\mathbf{z} = \mathbf{M}_3\mathbf{M}_1^{-1}. \tag{63}$$

Hence, substituting equation (52) and equation (62) in equation (53), we get:

$$\frac{d}{dr}\mathbf{U} = \frac{1}{r}\mathbf{G}_1\mathbf{U} + \frac{1}{r}\mathbf{G}_2\mathbf{z}\mathbf{U}, \tag{64}$$

$$\frac{d}{dr}\left(\mathbf{z}\mathbf{U}\right) = \frac{1}{r}\mathbf{G}_3\mathbf{U} - \frac{1}{r}\mathbf{G}_1^T\mathbf{z}\mathbf{U}. \tag{65}$$

Moreover, substituting equation (64) in equation (65) we derive the following differential matrix Riccati equation:

$$\frac{d}{dr}\mathbf{z} = \frac{1}{r}\left(\mathbf{G}_3 - \mathbf{G}_1^T\mathbf{z} - \mathbf{z}\mathbf{G}_1 - \mathbf{z}\mathbf{G}_2\mathbf{z}\right). \tag{66}$$

Using equation (62), the boundary conditions in equation (39) can be transformed in the initial and the stop conditions of the differential matrix Riccati equation in equation (66), as listed in Table 2.

	initial conditions	stop conditions
a) No loads	$\mathbf{z}(r_i) = \mathbf{0}$	$\det \mathbf{z}(r_0) = 0$
b) External pressure	$\mathbf{z}(r_i) = \mathbf{0}$	$\det\left[\mathbf{z}(r_0) - P\begin{pmatrix} G_{11} & G_{12} & G_{13} \\ 0 & 0 & 0 \\ 0 & 0 & 0 \end{pmatrix}\right] = 0$
c) Internal pressure	$\mathbf{z}(r_0) = \mathbf{0}$	$\det\left[\mathbf{z}(r_i) - P\begin{pmatrix} G_{11} & G_{12} & G_{13} \\ 0 & 0 & 0 \\ 0 & 0 & 0 \end{pmatrix}\right] = 0$

Table 2: Initial and stop conditions used to integrate numerically equation (66) in order to get the bifurcation parameters of the torsional instability.

In practice, we implement the following numerical procedure for solving the incremental problem based on the conditional impedance matrix. Fixing the initial aspect ratio H of the tube, and making outer iterations on the wavenumbers m and k_z, we integrate numerically equation (66) using the initial conditions in the first column in Table 2 and we iterate on the torsion rate γ until the stop condition in the second column of Table 2 is satisfied. In the next section, we present the resulting numerical results and we discuss the role of the axial and circumferential pre-stretches on the onset of helical buckling.

5 Numerical results

The numerical results of the linear stability analysis are presented in the following for each of the three different load scenarios under consideration. In order to elucidate the analysis of the numerical results, we present an illustrating example to show how we calculate the critical value of torsion rate and the associated circumferential and longitudinal modes at the onset of the torsional instability.

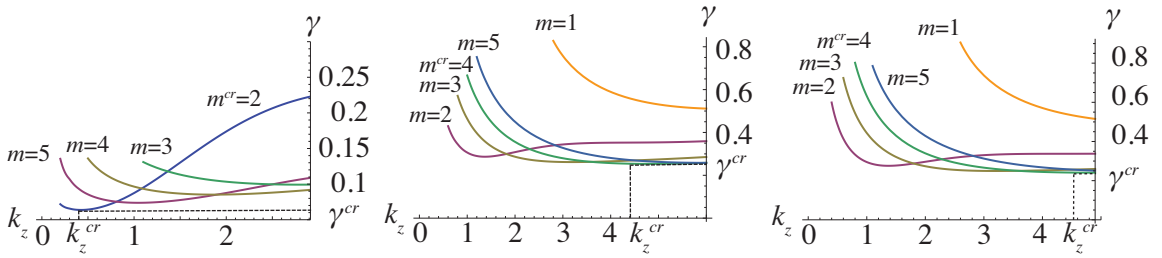

Figure 6: Critical torsion rates γ in function of the longitudinal mode k_z, plotted for different circumferential modes $m = 1, 2, 3, 4, 5$, obtained considering a) a stress-free cylindrical tube, b) a tube with an applied external or c) internal pressure. In each case, we set $H = 1.05$, $R_0 = 1$, $\mu = 1$ and in case b) and c), we calculate the pressure from equation (26) and equation (29) respectively, using $\beta = \pi/4$ and $\lambda_z = 1$. The absolute minimum among all the curves identifies the critical values for m^{cr}, k_z^{cr} and γ^{cr}.

In Figure 6, the bifurcation parameter γ is plotted against the longitudinal mode k_z and for different circumferential numbers m, for cylindrical tubes without external loads (Figure 6a), with external pressure P given by equation (26) (Figure 6b) and with internal pressure P given by equation (29) (Figure 6c), setting $H = 1.05$, $R_0 = 1$, $\mu = 1$, $\beta = \pi/4$, and $\lambda_z = 1$.

For each example, the critical value γ^{cr} corresponds to the absolute minimum among all the curves, whilst the corresponding m^{cr} and k_z^{cr} define the critical circumferential and longitudinal modes, respectively. For each class of boundary value problems, we find that both the critical circumferential and longitudinal modes depend on the initial aspect ratio.

Although the pressure is the control parameter in the cases (b) and (c), we use the functional relationships in equations (26, 29) to consider the pre-stretches as the order parameters of the helical buckling. In fact, the strategy of fixing P, and then calculating from equations (26, 29) one pre-stretch λ_θ or λ_z at any given H whilst keeping the other fixed, would give a pre-strain varying with H, and a direct comparison with the results of the case (a) would be difficult. Furthermore, in many biological tissues the in-vivo pressure is not always known, while the geometrical data and the pre-strains are measurable from *ex-vivo* cutting experiments. Accordingly, we investigate in the following paragraphs the role played by the circumferential and axial pre-stretches λ_θ and λ_z, respectively, on the onset of the torsional instability.

5.1 Effect of the circumferential pre-stretch

Here, the role played by the circumferential pre-stretch λ_θ, on the onset of the torsional instability is investigated. We recall that the circumferential pre-stretch depends on the initial angle $\beta < 2\pi$, as $\lambda_\theta = 2\pi/(2\pi - \beta)$. In Figure 7, the values of critical torsion rates γ^{cr} are plotted against the initial aspect ratio H, for different initial opening angles β and at fixed $\lambda_z = 1$.

The bifurcation parameters are shown in the case of traction-free cylindrical tubes (Figure 7a), tubes with applied external pressure P given by equation (26) (Figure 7b) or applied internal pressure P given by equation (29) (Figure 7c). The marginal stability curves show how, for a fixed H, an increase in the initial opening angle corresponds to an increase of the critical torsion rate. In the case of traction-free

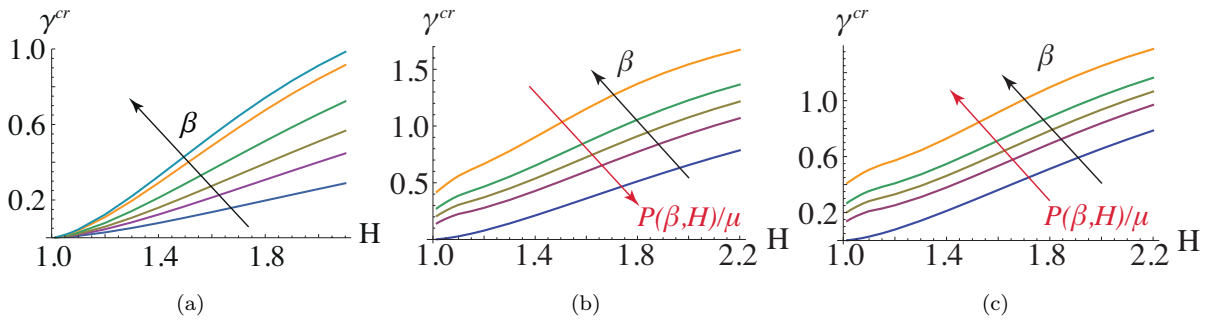

Figure 7: Critical values of torsion rate γ^{cr} plotted against the initial aspect ratio H at $\lambda_z = 1$, in three physical examples: traction-free (a) at $\beta = -\pi, -\pi/2, -\pi/4, 0, \pi/4, \pi/3$ applied external (b) and internal (c) pressure. In cases b) and c), we calculate the external and internal pressure P from equation (26) and equation (29), respectively, using $\beta = 0, \pi/6, \pi/4, \pi/3, \pi/2$.

cylindrical tubes, this effect becomes more relevant for thicker tubes, while the critical torsion $\gamma^{cr} \to 0$ for $H \to 1$. When a pressure is applied on the external or the internal surface of the cylindrical tube, instead, the critical torsion rate for $H \to 1$ approaches a finite value depending on β.

In Figure 8, the values of the critical longitudinal mode k_z^{cr} are plotted as functions of the initial

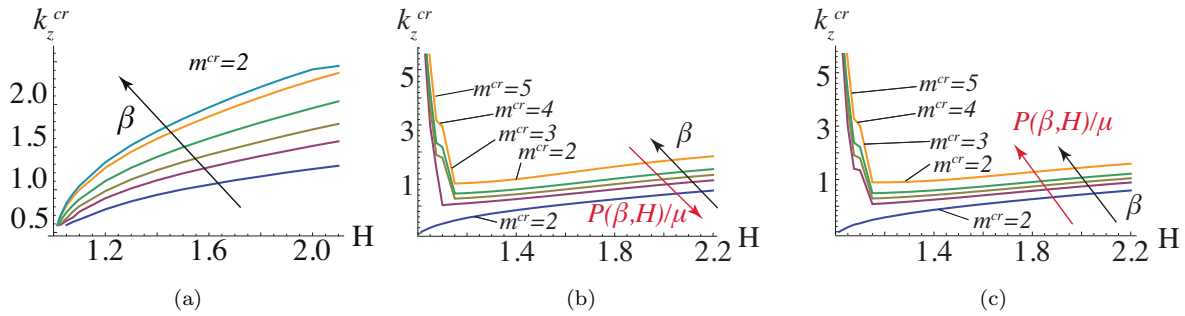

Figure 8: Critical values of longitudinal mode k_z^{cr} plotted against the initial aspect ratio H at $\lambda_z = 1$, in three physical examples: traction-free (a) at $\beta = -\pi, -\pi/2, -\pi/4, 0, \pi/4, \pi/3$, applied external (b) and internal (c) pressure. In the cases b) and c) the pressure P is calculated from equation (26) and equation (29), respectively, at $\beta = 0, \pi/6, \pi/4, \pi/3, \pi/2$. The solid black lines indicate the related value of m^{cr} for each branch of the curves.

aspect ratio H at different initial opening angles and at fixed $\lambda_z = 1$, for traction-free cylindrical tubes (Figure 8a), tubes with applied external pressure (Figure 8b) or applied internal pressure (Figure 8c). The critical circumferential modes are also depicted at different range of H, showing that when a traction free boundary condition is considered, the circumferential mode is always $m^{cr} = 2$. The same behavior is observed in the case of applied external or internal pressure, when $\lambda_\theta = 1$. Otherwise, when $\lambda_\theta \neq 1$, tubes with $H \geq 1.2$ exhibit $m^{cr} = 2$, while thinner tubes have higher critical circumferential wavenumbers.
On the other hand, for a fixed initial aspect ratio, the absolute value of the critical longitudinal mode increases as the initial opening angle increases. Moreover, thin tubes ($1 < H < 1.1$) select higher longitudinal critical wavenumbers than thick tubes.

5.2 Effect of the axial pre-stretch

In this section, the role played by the pre-stretch λ_z on the onset of torsional instabilities is analyzed. In Figure 9, the critical torsion rates γ^{cr} are plotted against the initial aspect ratio H, for different pre-stretches λ_z at fixed $\beta = \pi/6$. The marginal stability curves are depicted for traction-free cylindrical

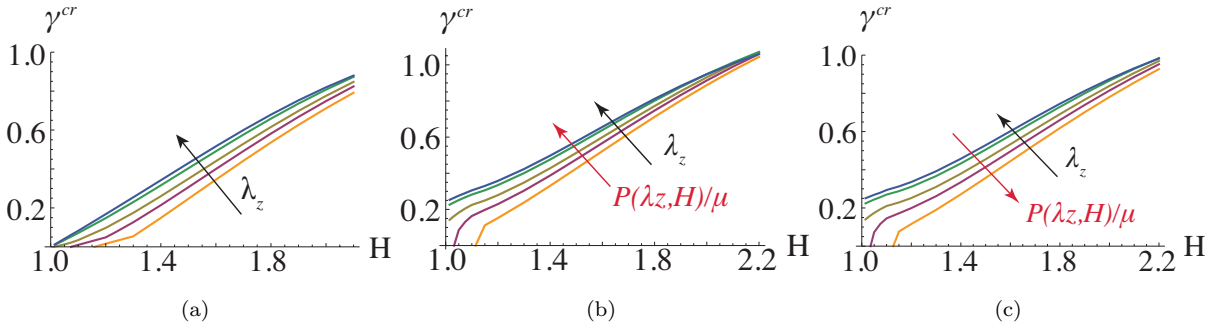

Figure 9: Critical values of torsion rate γ^{cr} plotted against the initial aspect ratio H for three sets of boundary conditions: traction-free tube (a), applied external (b) or internal (c) pressure for $\lambda_z = 0.9, 0.95, 1, 1.1, 1.2$, and $\beta = \pi/6$. In the cases b) and c), we calculate the external and internal pressure P from equation (26) and equation (29), respectively, at the given values of λ_z.

tubes (Figure 9a), tubes with applied external pressure given by equation (26) (Figure 9b) and with applied internal pressure given by equation (29) (Figure 9c). At fixed initial aspect ratio, the critical values of torsion rates increase as λ_z increases, showing how a cylindrical tube under a finite compression becomes unstable at lower torsion rates than one subjected to a finite extension. Furthermore, thin tubes have always lower values of critical torsion rate than thick tubes.
In Figure 10, the critical longitudinal modes are depicted for traction-free cylindrical tubes (Figure 10a), cylindrical tubes with applied external (Figure 10b) and internal (Figure 10c) pressure. The critical circumferential modes are also displayed for the three cases. The marginal stability curves highlight that

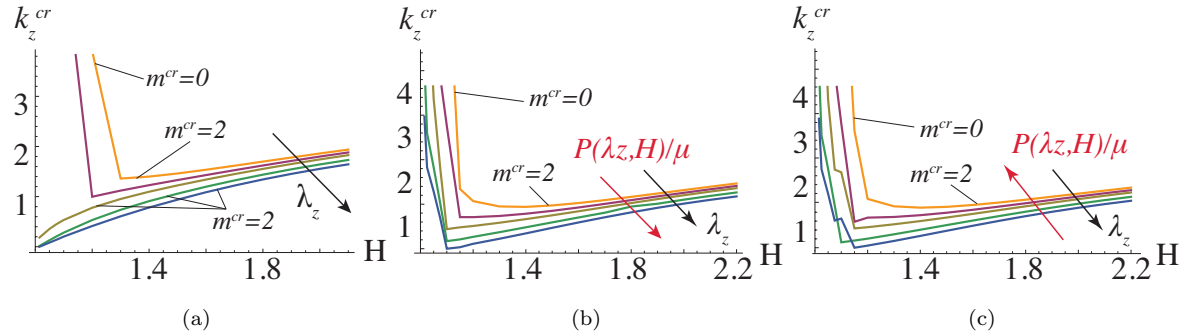

Figure 10: Critical values of longitudinal mode k_z^{cr} plotted against the initial aspect ratio H in three physical examples: traction-free (a), applied external (b) and internal (c) pressure at $\lambda_z = 0.9, 0.95, 1, 1.1, 1.2$, and $\beta = \pi/6$. In the cases b) and c) the pressure P is calculated from equation (26) and equation (29), respectively, at the given values of λ_z. The solid black lines indicate the related value of m^{cr} for each branch of the curves.

tubes under axial compression select higher longitudinal modes than tubes under axial extension, while $m^{cr} = 2$ for thick tubes. For $\lambda_z < 1$, the axial compression provokes a *barreling* instability, corresponding

$m^{cr} = 0$, in thin tubes without any torsion. Although out of the scope of this work, it should be recalled that in this case other asymmetric modes can occur for the buckling of a compressed tube with guided-guided end conditions [25].

6 Discussions

We have investigated the torsional instabilities which can emerge when a soft, residually-stressed cylindrical tube is subjected to a finite torsion. The model accounts for an initial opening angle β, which defines the circumferential pre-stretch $\lambda_\theta = 2\pi/(2\pi - \beta)$, and for a uniform axial pre-stretch λ_z, in order to represent the three-dimensional distribution of residual strains that is observed in living tubular tissues, such as arteries.

In Section 2, we have presented the geometry and the kinematics of the elastic model. Considering an incompressible neo-Hookean material, in Section 3 we derived the basic axisymmetric solutions for the three different sets of boundary conditions. As depicted in Figure 2, we considered: traction-free boundary conditions at both internal and external surfaces (a), an applied pressure load P given by equation (26) at the external surface (b) or an applied pressure load P given by equation (29) at the internal surface (c). In Section 4, we performed a linear stability analysis using the method of small deformations superposed on finite strains. The incremental elastic problem has been derived using the Stroh formulation. Even if previous works [12, 14] also transformed the incremental equations in a system of ODEs, they did not use the optimal, Hamiltonian form based on the Stroh formalism [26]. The incremental solution has been calculated using a numerical procedure based on the surface impedance method, which allows to rewrite the Stroh problem as a differential matrix Riccati equation with given initial conditions. The numerical results have been presented in Section 5, reporting the marginal stability curves for the critical torsion rate γ^{cr}. An illustration of the deformed tube at the onset of the torsional instability is depicted in Figure 5. As illustrated in Figure 6, the helical buckling is characterized by critical circumferential and longitudinal modes, m^{cr} and k^{cr}, respectively, depending both on the initial thickness of the tube and on the existing-pre-stretches. This confirms that the torsional instability in soft tubes strongly differs from the one for solid cylinders, which is characterized by a critical mode $m = 1$ [11], with the initial formation of a kink nonlinearly evolving into a knot [9].

Moreover, we find that the critical torsion rate γ^{cr} increases with an increasing initial thickness of the hollow cylinder in accordance with the experimental results of Wang and Ertepinar [14] on stress-free rubber tubes. However, whilst Wang and Ertepinar analyzed such data by incorrectly using a simplified model based on a homogeneous basic deformation, we show here that the inhomogeneous displacements fields in equations (4, 6) must be considered in order to satisfy the stress-free boundary conditions for an incompressible material. Furthermore, when a traction-free boundary condition is considered, the circumferential mode is independent of the thickness of the tube and is always $m^{cr} = 2$ for $\lambda_z \geq 1$.

Another novel aspect of this study concerns the investigation of the effects of the circumferential and axial pre-strains on the onset of the torsional instability. The marginal stability curves in Figures 7-10 have shown that both the critical torsion rate and the axial wavenumber increase for increasing circumferential and axial pre-stretches. In particular, such a result on the axial wavenumber is in accordance with the results on torsional instabilities in solid cylinders [11, 12].

Finally, in Figure 11 we compare the critical torsion rates and the critical circumferential and longitudinal modes for the three sets of boundary conditions that we have considered. As expected, we find that a tube without any loads is the most unstable configuration with respect to torsional instabilities, while the most stable configuration is always the externally pressured tube. Future work will be focused on investigating the role of pressure as an independent control parameter of the stability properties of the tube, without assuming any functional dependence on the residual strains.

In conclusion, we have determined the occurrence of torsional instabilities in soft cylindrical tubes with circumferential and axial pre-stretches, considering three different sets of boundary conditions. Using a robust numerical procedure based on the matrix Riccati equations of the incremental problem, we have

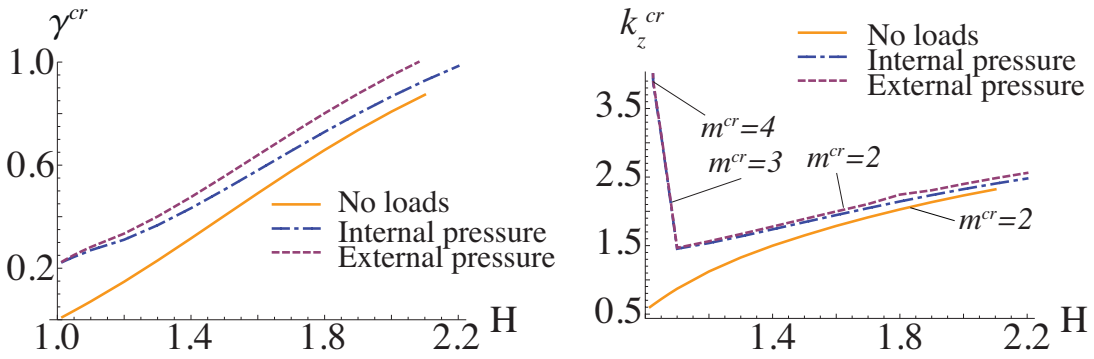

Figure 11: Critical values of the torsion rate γ^{cr} (left) and the longitudinal mode k_z^{cr} (right) plotted against the initial aspect ratio H, considering stress-free conditions (orange, solid), and applied external (purple, dashed) or internal (blue, dash-dot) pressure, with $\lambda_z = 1$, and $\beta = \pi/6$. The blue and purple lines are obtained by calculating the external and internal pressures from equation (26) and equation (29), respectively. The solid black lines indicate the related value of m^{cr} for each branch of the curves.

calculated the order parameters of the elastic bifurcation, deriving the critical torsion rates and the associated critical modes. This work demonstrates that the distribution of residual strains plays a key role on the onset of torsional instabilities in soft hollow cylinders, which is of utmost importance when studying the biomechanical behavior of soft tubular tissues.

Acknowledgements

Partial funding by the European Community grant ERG-256605 (FP7 program), the INSERM grant OTPJ12U170 (Plan Cancer), are gratefully acknowledged. The authors also thank the anonymous referees for constructive comments on an earlier version of the paper.

References

[1] Rivlin RS. Large elastic deformations of isotropic materials. IV. Further developments of the general theory. *Philos Tr R Soc S-A* 1948; 241: 379-397.

[2] Rivlin RS. A note on the torsion of an incompressible highly elastic cylinder. *Math Proc Cambridge* 1949; 45(3): 485-487.

[3] Ericksen LA. Deformations possible in every isotropic, incompressible, perfectly elastic body. *Z Angew Math Phys* 1954; 5: 466-489.

[4] Truesdell C and Noll W. *The non-linear field theories of mechanics.* In: Flügge W. Handbuch der Physik, III/3. Berlin-Heidelberg-New York: Springer, 1965.

[5] Carroll MM. Controllable deformations of incompressible simple materials. *Int J Eng Sci* 1967; 5: 515-525.

[6] Fosdick RL. Dynamically possible motions of incompressible, isotropic, simple materials. *Arch Rational Mech Anal* 1968; 29: 272-278.

[7] Rivlin RS. Large elastic deformations of isotropic materials. VI. Further results in the theory of torsion, shear and flexure. *Philos Tr R Soc S-A* 1949; 242: 173-195.

[8] Ogden RW, Chadwick P and Haddon EW. Combined axial and torsional shear of a tube of incompressible isotropic elastic material. *Q J Mech Appl Math* 1973; 26(1): 23-41

[9] Gent AN and Hua KC. Torsional instability of stretched rubber cylinders. *Int J Nonlin Mech* 2004; 39: 433-439.

[10] Yamaki N. *Elastic stability of circular cylindrical shells.* Amsterdam: North-Holland, 1984.

[11] Green AE and Spencer AJM. The stability of a circular cylinder under finite extension and torsion. *J Math Phys* 1959; 37: 316-338.

[12] Duka ED, England AH and Spencer AJM. Bifurcation of a solid circular cylinder under finite extension and torsion. *Acta Mech* 1993; 98: 107-121.

[13] Flügge W. *Stresses in shells.* 2nd ed. Berlin Heidelberg New York: Springer-Verlag, 1973.

[14] Ertepinar A and Wang ASD. Torsional buckling of an elastic thick-walled tube made of rubber-like material. *Int J Solids Struct* 1975; 11: 329-337.

[15] Holzapfel GA and Ogden RW. Modelling the layer-specific three-dimensional residual stresses in arteries, with an application to the human aorta. *J R Soc Interface* 2010; 7: 787-799.

[16] Ciarletta P and Ben Amar M. Pattern formation in fiber-reinforced tubular tissues: Folding and segmentation during epithelial growth. *J Mech Phys Solids* 2012; 60: 525-537.

[17] Ogden RW. *Non-linear elastic deformations.* New York: Ellis Horwood Chirchester, 1997.

[18] Hoger A. On the residual stress possible in an elastic body with material symmetry. *Arch Ration Mech Anal* 1985; 88: 271-290.

[19] Destrade M, Murphy JG and Ogden RW. On deforming a sector of circular cylindrical tube into an intact tube: existence, uniqueness and stability. *Int J Eng Sci* 2010; 48: 1212-1224.

[20] Takamizawa K and Hayashi K. Strain energy density function and uniform strain hypothesis for arterial mechanics. *J Biomech*, 1987; 20(1), 7–17.

[21] Stroh AN. Steady state problems in anisotropic elasticity. *J Math Phys* 1962; 41: 77-103.

[22] Biryukov SV. Impedance method in the theory of elastic surface wave. *Sov Phys Acoust* 1985; 31: 350-354.

[23] Norris AN and Shuvalov AL. Wave impedance matrices for cylindrically anisotropic radially inhomogeneous elastic solids. *Quart J Mech Appl Math* 2010; 63: 401-435.

[24] Destrade M, Ní Annaidh A and Coman C. Bending instabilities of soft biological tissues. *Int J Solids Struct* 2009; 46: 4322-4330.

[25] De Pascalis R, Destrade M and Goriely A. Nonlinear correction to the Euler buckling formula for compressed cylinders with guided-guided end conditions. *J Elast* 2011; 102: 191-200.

[26] Fu YB. Hamiltonian interpretation of the Stroh formalism in anisotropic elasticity. *Proc Roy Soc Lond A* 2007; 463: 3073-3087.